

# The GalSim lensing engine

## ABSTRACT

This document describes the GalSim “lensing engine” for drawing shears randomly according to a user-specified shear power spectrum. It includes a brief description of the theory behind shear power spectra, the connection between the usual continuous description of the theory versus our representation in terms of the discrete Fourier transform, and a validation of the outputs for several test cases.

## Contents

<b>1</b>	<b>Introduction</b>	<b>2</b>
<b>2</b>	<b>Theory</b>	<b>2</b>
2.1	Continuous representation . . . . .	2
2.2	Representation on grids . . . . .	3
<b>3</b>	<b>Representing continuous fields using the Discrete Fourier Transform</b>	<b>4</b>
3.1	Conventions . . . . .	5
3.2	Fourier transform properties . . . . .	5
3.3	The Fourier transform of discrete samples of the power spectra . . . . .	6
3.4	The Fourier transform of discrete, finite samples of the power spectra . . . . .	7
<b>4</b>	<b>Comparison software</b>	<b>9</b>
<b>5</b>	<b>Tests of variances</b>	<b>9</b>
5.1	General considerations . . . . .	10
5.2	Variance for Gaussian $P(k)$ . . . . .	10
5.3	Variance for flat $P(k)$ . . . . .	11
<b>6</b>	<b>Test of full <math>P(k)</math></b>	<b>12</b>

## 7 Shear power on larger scales than our grid

17

### 1. Introduction

The lensing engine (in `galsim/lensing.py`) is the part of GalSim that is supposed to draw shears randomly according to a user-specified power spectrum. In this document, we begin with a brief description of the theory behind shear power spectra (§2), and then clarify the following issues:

1. How does the discrete representation that we use (on a grid) relate to the standard formulation of the theory, which uses continuous representations? (§3)
2. Are our outputs consistent with expectations?
  - How does it compare with another standard piece of software that generates shears using a different formalism? (§4)
  - Is the normalization (expressed as a variance) correct? (§5)
  - Does the variance behave appropriately when the grid size and spacing is changed? (§5)
  - Does the full  $P(k)$  of the shears that were generated agree with our expectations? Does the result behave appropriately when the grid size and spacing is changed? (§6)
  - Is the behavior appropriate when inputting only  $E$  mode power, only  $B$  mode power, and both  $E$  and  $B$  mode power? (§6)
3. We should consider the impact of our current choice to force  $P(k=0) = 0$ , which effectively says there is no cosmic variance. (§7)

### 2. Theory

#### 2.1. Continuous representation

The lensing engine requires a shear power spectrum,  $P(k)$ , and assumes we are in the flat-sky limit. Many standard references regarding lensing power spectra work in terms of the spherical harmonics  $\ell$ , with the power spectrum denoted  $C_\ell$ . In the flat-sky limit we can simply swap  $\ell$  with  $k$  and  $C_\ell$  with  $P(k)$ . It is standard practice to plot a dimensionless quantity  $\Delta^2$  defined as

$$\Delta^2 = \frac{\ell(\ell+1)C_\ell}{2\pi} \equiv \frac{k^2 P(k)}{2\pi}. \quad (1)$$

If we identify pairs of galaxies separated by an angle  $\theta$  on the sky, and compute their shears in a coordinate system defined along the vector connecting them ( $\gamma_+$ ) and at 45 degrees with respect

to it ( $\gamma_{\times}$ ), then we can estimate correlation functions of the  $\gamma_{+}$  and  $\gamma_{\times}$  values, which we will call  $\xi_{++}$  and  $\xi_{\times\times}$ . Then the standard cosmological correlation functions  $\xi_{\pm}$  are defined as

$$\xi_{\pm}(\theta) = \xi_{++}(\theta) \pm \xi_{\times\times}(\theta) \quad (2)$$

$$= \frac{1}{2\pi} \int_0^{\infty} k \, dk P(k) J_{0/4}(k\theta) \quad (3)$$

where  $J_{0/4}$  denotes the 0th and 4th Bessel function of the first kind, as is appropriate for  $\xi_{+}$  and  $\xi_{-}$ , respectively. Since correlation functions are dimensionless, we immediately see that  $P(k)$  has dimensions of  $\text{angle}^2$ .

The variance of the shear values for all of our galaxies is the zero-lag value of  $\xi_{+}$ ,

$$\text{Var}(\gamma) = \xi_{+}(\theta = 0) = \langle g_1^2 + g_2^2 \rangle. \quad (4)$$

Combining Eqs. 3 and 4, we can write the shear variance in terms of the power spectrum

$$\text{Var}(\gamma) = \frac{1}{2\pi} \int_0^{\infty} k \, dk P(k), \quad (5)$$

which essentially says the shear variance is the power integrated over the allowed area in  $k$  space.

## 2.2. Representation on grids

We will have to modify the above formalism to account for the fact that all of our calculations use a discrete representation on a finite grid. The real-space grid is defined by

$$L = \text{length of grid along one dimension (angular units)} \quad (6)$$

$$d = \text{spacing between grid points (angular units)} \quad (7)$$

$$N = \text{number of grid points along one dimension} = L/d. \quad (8)$$

There is a comparable grid in Fourier-space (i.e., same  $N$ ). Given the parameters of the real-space grid, the  $k_{\min}$  along one dimension is  $2\pi/L$ , so we can think of this quantity as the grid spacing in Fourier space, i.e.,  $k_{\min} = \Delta k$ . This value of  $k_{\min}$  corresponds to a Fourier mode that exactly fits inside of our square grid (in one dimension). The  $k$  range, again in one dimension, is from  $k_1 = -\pi/d$  to  $\pi/d$ , i.e.,  $|k_1| < k_{\max} = \pi/d$ . This corresponds to a mode that is sampled exactly twice (the minimum possible) given our choice of grid spacing. For the two-dimensional grid, the maximum value of  $|k|$  is then  $\sqrt{2}\pi/d$ .

Given the Fourier-space grid, the lensing engine works in the simplest possible way: it samples the power  $P(k)$  at the values of  $(k_1, k_2)$  on the grid by obtaining  $P((k_1^2 + k_2^2)^{1/2})$ ; draws random amplitudes from a Gaussian based on the square root of  $P(k)$ ; and Fourier transforms this back to our square real-space grid with periodic boundary conditions to obtain the real-space shear field.

For a given grid point in Fourier space, it is somewhat a matter of taste as to whether it is considered to start at that  $k$  and extend to  $k + \Delta k$ , or whether it goes from  $k - \Delta k/2$  to  $k + \Delta k/2$ . For the examples we will consider, the difference between these two options is typically of order 1%. In practice, the choice of convention just shifts the limits of integration in the equations below by at most  $\Delta k$ .

In the context of power spectra for gridded quantities, instead of using Eq. 5 it is more useful to think in terms of the 2D integral in Cartesian coordinates

$$\text{Var}(\gamma) = \frac{1}{(2\pi)^2} \int_{-\infty}^{\infty} dk_1 dk_2 P(k_1, k_2). \quad (9)$$

Note that this equation assumes that our grid is infinite and  $P(k)$  is defined for all  $k$ . With a limited  $k$  range, and with the power spectrum forced to  $P(0) = 0$  (see §7 for more discussion of this), we can rewrite Eq. 9 as

$$\text{Var}(\gamma) = \frac{4}{(2\pi)^2} \left[ \int_0^{k_{\max}} \int_0^{k_{\max}} dk_1 dk_2 P(k) - \int_0^{k_{\min}} \int_0^{k_{\min}} dk_1 dk_2 P(k) \right]. \quad (10)$$

Here the factor of 4 compensates for the quadrants that are not represented explicitly (i.e., negative  $k_1$  and/or  $k_2$  values).

Another interesting point about gridded quantities is that it is not clear that we can enforce/check behavior of  $\text{Var}(\gamma_1)$  or  $\text{Var}(\gamma_2)$ , particularly if there is a lot of shear power at small  $k$ . Probably we should only expect normal behavior for  $\text{Var}(\gamma)$ , but it's still worth verifying this explicitly in Sec. 5.

In the limit that our power spectrum drops to zero at  $k_{\max}$ , and that there is not too much power in the range  $0 < k < k_{\min}$  relative to that in  $k_{\min} < k < k_{\max}$ , Eqs. 5, 9, and 10 should all give the same answer.

The above equations just include  $P(k)$ , but in principle there can be two such functions,  $P_E$  and  $P_B$ . These should simply be summed in Eqs. 5, 9, and 10.

### 3. Representing continuous fields using the Discrete Fourier Transform

This section includes is the formalism describing what the GalSim lensing engine is actually doing when representing shear fields as discrete fields defined on a finite grid, as opposed to the continuous representation in §2.

### 3.1. Conventions

The definition of the correlation function in equation (3) employs the *angular frequency, non-unitary*<sup>1</sup> definition of the (1D) Fourier transform:

$$\tilde{f}(k) = \int_{-\infty}^{\infty} f(x) e^{-ikx} dx \equiv \mathcal{F}\{f(x)\}; \quad (11)$$

$$f(x) = \frac{1}{2\pi} \int_{-\infty}^{\infty} \tilde{f}(k) e^{ikx} dk \equiv \mathcal{F}^{-1}\{\tilde{f}(k)\}, \quad (12)$$

with the usual simple generalizations to two or more dimensions.

The standard results in Discrete Fourier Transform (DFT) and its halfway-house the Discrete Time Fourier Transform (DTFT) are all derived under the unitary (i.e. without asymmetric prefactors of  $1/2\pi$ ) convention in the online literature, adding to the complexity of interpretation. In the next section, we present some of the standard results of Fourier theory using the angular frequency, non-unitary convention above, since we will require them in Section 3.3.

### 3.2. Fourier transform properties

It can be readily shown that if we define  $g(xL) \equiv f(x)$ , the following well-known identity holds under our Fourier transform convention:

$$\mathcal{F}\{g(xL)\} = \frac{1}{L} \tilde{g}\left(\frac{k}{L}\right). \quad (13)$$

If we further define  $s(h+x) \equiv g(x)$  then it is straightforward to show that

$$\mathcal{F}\{s(h+x)\} = e^{ikh} \tilde{s}(k). \quad (14)$$

Here we begin to get divergent results between conventions: there is an additional factor of  $2\pi$  in the exponent when this property of FTs is expressed using the normal frequency convention.

The most important result for approximating continuous functions using DFTs is the Poisson summation formula, which under our conventions may be stated as

$$\sum_{n=-\infty}^{\infty} f(n) = \sum_{q=-\infty}^{\infty} \tilde{f}(2\pi q) \quad (15)$$

for integers  $n$  and  $q$ . This result can be derived by writing the expression for the inverse Fourier transform of  $\tilde{f}(2\pi q)$  and considering the Fourier series expansion of the periodic Dirac comb function

$$\text{III}_L(x) = \sum_{n=-\infty}^{\infty} \delta(x - nL). \quad (16)$$

---

<sup>1</sup>According to the paradigm described in [http://en.wikipedia.org/wiki/Fourier\\_transform#Other\\_conventions](http://en.wikipedia.org/wiki/Fourier_transform#Other_conventions)

It should be noted that in the normal frequency, unitary transform convention form of the Poisson summation formula the  $2\pi$  within  $\tilde{f}(2\pi q)$  is absent. Using equation (13) we then find

$$\sum_{n=-\infty}^{\infty} f(nL) = \frac{1}{L} \sum_{q=-\infty}^{\infty} \tilde{f}\left(\frac{2\pi q}{L}\right), \quad (17)$$

which can be modified further using equation (14) to give the most useful expression of the Poisson summation formula:

$$\sum_{n=-\infty}^{\infty} f(nL + x) = \frac{1}{L} \sum_{q=-\infty}^{\infty} \tilde{f}\left(\frac{2\pi q}{L}\right) e^{i2\pi x q/L}. \quad (18)$$

If we define  $\Delta k \equiv k_{\min} = 2\pi/L$  we can also write this as

$$\sum_{n=-\infty}^{\infty} f\left(\frac{2\pi n}{\Delta k} + x\right) = \left(\frac{\Delta k}{2\pi}\right) \sum_{q=-\infty}^{\infty} \tilde{f}(q\Delta k) e^{ix\Delta k q}. \quad (19)$$

These results give us most of what we need to understand DFTs with the non-unitary Fourier transform convention commonly adopted for weak lensing power spectra in the flat sky approximation.

### 3.3. The Fourier transform of discrete samples of the power spectra

In what follows we are going to derive results only for the  $\xi_+$  correlation function of equation (3). This will not impact the understanding of how  $P(k)$  is approximated using DFTs, but allows us to replace  $\xi_{\pm}$  and  $J_{0/4}(k\theta)$  in equation (3) with the simpler  $\xi_+$  and  $J_0$ , respectively. We will just be aware subsequently that real ellipticity fields have two components, to be treated as described by equation (3).

The inverse Fourier transform of  $P(k)$  to give  $\xi_+(\theta)$  may be written in Cartesian coordinates as

$$\xi_+(\theta_1, \theta_2) = \frac{1}{(2\pi)^2} \iint_{-\infty}^{\infty} P(k_1, k_2) e^{i(k_1\theta_1 + k_2\theta_2)} dk_1 dk_2. \quad (20)$$

The relation between this and equation (3) makes use of Bessel's first integral:

$$J_n(z) = \frac{i^{-n}}{\pi} \int_0^{\pi} e^{iz \cos \theta} \cos(n\theta) d\theta. \quad (21)$$

What happens if we only have finite samples of  $P(k_1, k_2)$ ? To answer that, let us define the following function:

$$P_{\Delta k}[q, p] \equiv (\Delta k)^2 P(q\Delta k, p\Delta k). \quad (22)$$

As here, we will use square brackets to denote functions with discrete, integer input variables. We will also use indices  $n, m$  in real space summations and  $q, p$  in Fourier space ( $i, j$  are awkward due to the common notations for  $\sqrt{-1}$ ). Let us also define the 2D Dirac comb function in Fourier space

$$\mathbb{I}_{\Delta k}^2(k_1, k_2) = \sum_{q=-\infty}^{\infty} \delta(k_1 - q\Delta k) \sum_{p=-\infty}^{\infty} \delta(k_2 - p\Delta k). \quad (23)$$

It can then be shown that

$$\begin{aligned}
& \mathcal{F}^{-1} \left\{ \sum_{q,p=-\infty}^{\infty} \delta(k_1 - q\Delta k) \delta(k_2 - p\Delta k) P_{\Delta k}[q,p] \right\} \\
&= \mathcal{F}^{-1} \{ P(k_1, k_2) \cdot (\Delta k)^2 \text{III}_{\Delta k}^2(k_1, k_2) \} \\
&= \mathcal{F}^{-1} \{ P(k_1, k_2) \} * \mathcal{F}^{-1} \{ (\Delta k)^2 \text{III}_{\Delta k}^2(k_1, k_2) \} \\
&= \xi_+(\theta_1, \theta_2) * \left\{ \sum_{n=-\infty}^{\infty} \delta\left(\theta_1 - \frac{2\pi n}{\Delta k}\right) \sum_{m=-\infty}^{\infty} \delta\left(\theta_2 - \frac{2\pi m}{\Delta k}\right) \right\} \\
&= \sum_{n,m=-\infty}^{\infty} \xi_+\left(\theta_1 - \frac{2\pi n}{\Delta k}, \theta_2 - \frac{2\pi m}{\Delta k}\right) \tag{24}
\end{aligned}$$

Here we have again made use of the Fourier series expression for the Dirac comb function, and employed the convolution theorem (convolution denoted with  $*$ ). We note that the final expression (24) is still continuous, but describes an infinite, periodic summation (of period  $L = 2\pi/\Delta k$ ) of copies of the correlation function  $\xi_+$ . For sufficiently small  $\Delta k$ , these copies may be well-enough spaced in the real domain to learn much about  $\xi_+(\theta_1, \theta_2)$  in the non-overlapping regions.

We therefore define this function as

$$\xi_{\frac{2\pi}{\Delta k}}(\theta_1, \theta_2) \equiv \sum_{n=-\infty}^{\infty} \xi_+\left(\theta_1 - \frac{2\pi n}{\Delta k}, \theta_2 - \frac{2\pi m}{\Delta k}\right). \tag{25}$$

Using the expression of the Poisson summation formula in equation (19), we can also write the result

$$\xi_{\frac{2\pi}{\Delta k}}(\theta_1, \theta_2) = \sum_{q,p=-\infty}^{\infty} \left(\frac{\Delta k}{2\pi}\right)^2 P(q\Delta k, p\Delta k) e^{i\Delta k(\theta_1 q + \theta_2 p)} = \frac{1}{(2\pi)^2} \sum_{q,p=-\infty}^{\infty} P_{\Delta k}[q,p] e^{i\Delta k(\theta_1 q + \theta_2 p)} \tag{26}$$

(which, like the Poisson summation formula, can also be shown using equation (24) and substituting the Fourier series expression for  $\text{III}_{\Delta k}^2$ ). This is the expression for the inverse of what is known as the Discrete Time Fourier Transform (DTFT), although this result is normally derived using unitary conventions for the transform pair. Note that the terms  $P_{\Delta k}[q,p]$  are dimensionless, being composed of  $(\Delta k)^2 = (2\pi/L)^2$  multiplied by the samples  $P(q\Delta k, p\Delta k)$  of the power  $P(k_1, k_2)$  (with dimensions of angle<sup>2</sup>).

One intuitive way of looking at the approximation of equation (20) for the case of discretely sampled  $P(k_1, k_2)$  is that the terms in the discrete sum should be considered as *impulses* of area  $(\Delta k)^2$  and height  $P(q\Delta k, p\Delta k)$ .

### 3.4. The Fourier transform of discrete, finite samples of the power spectra

The expression in equation (26) is periodic with period  $2\pi/\Delta k = L$ . All of the information it contains about  $\xi_+(\theta_1, \theta_2)$  is therefore also contained in one period of the function only. For

approximating this information discretely, as desired in numerical analysis, we can imagine taking  $N$  equally spaced samples of the function in equation (26) along a single period  $L$  in each dimension (leading to  $N^2$  samples total since we are working in 2D). These samples are therefore separated by  $\Delta\theta = 2\pi/\Delta k N = d$  in real space, and we define the sampled function itself as

$$\xi_{\Delta\theta}[n, m] \equiv \xi_{\frac{2\pi}{\Delta k}}(n\Delta\theta, m\Delta\theta) = \frac{1}{(2\pi)^2} \sum_{q, p=-\infty}^{\infty} P_{\Delta k}[q, p] e^{i2\pi(qn+pm)/N}, \quad (27)$$

for the integer indices  $n, m = 0, 1, \dots, N-1$ , by substitution into equation (26). Using the periodicity of the exponential term in the expression above, this may be written as

$$\xi_{\Delta\theta}[n, m] = \frac{1}{(2\pi)^2} \sum_{q, p=0}^{N-1} P_N[q, p] e^{i2\pi(qn+pm)/N} \quad (28)$$

where we have defined

$$P_N[q, p] \equiv \sum_{i, j=-\infty}^{\infty} P_{\Delta k}[q - iN, p - jN]. \quad (29)$$

Needless to say, in order to be able to calculate the values of  $P_N[q, p]$  in practice we must also truncate the  $P_{\Delta k}$  sequence to be finite in length. A *very* common choice is to use the same number  $N$  of samples in both real and Fourier space: this is also efficient, as it allows the direct use of the Fast Fourier Transform algorithm. We will say a little more about this below.

Choosing to use only  $N$  samples from  $P_{\Delta k}$  then gives us a somewhat more familiar expression for the inverse Discrete Fourier Transform (DFT), written here for the non-unitary Fourier transform convention:

$$\xi_{\Delta\theta}[n, m] = \frac{1}{(2\pi)^2} \sum_{q, p=0}^{N-1} P_{\Delta k}[q, p] e^{i2\pi(qn+pm)/N}. \quad (30)$$

The overwhelmingly more common definition of the inverse DFT, and that adopted by NumPy, instead reads as:

$$f[n, m] = \text{numpy.fft.ifft2}(\tilde{f}[p, q]) \equiv \frac{1}{N^2} \sum_{q, p=0}^{N-1} \tilde{f}[q, p] e^{i2\pi(qn+pm)/N}, \quad (\text{NumPy convention}) \quad (31)$$

where the factor of  $1/N^2$  is a convention commonly found in DFT implementations, and ensures that the DFT followed by the inverse DFT yields the original, input array.

We must use the convention of equation (31) for performing the calculation within the code, and so this means that we must attempt to account for the factors of  $2\pi$ ,  $N$  and  $\Delta k$  ourselves. Let us begin with the user specifying the key dimensions of the problem  $L$  and  $d = \Delta\theta$  at the outset, as assumed in Section 2, sensibly chosen (of course) so that  $N = L/\Delta\theta$  is an integer. These choices also set  $\Delta k = 2\pi/L$ . Beginning with equation (30), we may re-express the convenient  $P_{\Delta k}[q, p]$  as



samples of the dimensional  $P(k_1, k_2)$  once again:

$$\xi_{\Delta\theta}[n, m] = \frac{1}{(2\pi)^2} \sum_{q,p=0}^{N-1} P_{\Delta k}[q, p] e^{i2\pi(qn+pm)/N} \quad (32)$$

$$= \frac{1}{(2\pi)^2} \times \frac{(2\pi)^2}{L^2} \sum_{q,p=0}^{N-1} P(q\Delta k, p\Delta k) e^{i2\pi(qn+pm)/N} \quad (33)$$

$$= \frac{1}{L^2} \sum_{q,p=0}^{N-1} P(q\Delta k, p\Delta k) e^{i2\pi(qn+pm)/N} \quad (34)$$

$$= \text{numpy.fft.ifft2} [P(q\Delta k, q\Delta k)/(\Delta\theta)^2] . \quad (35)$$

This equation explains why we require a division of the amplitudes by  $d = \Delta\theta$  in the lensing engine. Dimensional analysis tells us that we require a division by something with dimensions of angle, but this equation is justification for exactly what angle is used.

Finally, we said we would say little more about the implications of the choice to use  $N$  as the number of samples in *both* real and Fourier space, the final step in arriving at equation (30). This choice ensures the close interrelation of  $N$ ,  $L$  and the grid spacings  $\Delta\theta$ ,  $\Delta k$ . The use of discrete, periodic sampling to represent continuous, non-periodic functions is only an approximation, and one that depends heavily on good choices of these interrelated sampling parameters.

The two effects that must be minimized for a good approximation are of course aliasing and unwanted ‘overlapping’ of functions in either real or Fourier space due to the sampled, periodic representation inherent in the DFT. Adequately sampling our functions, and zero-padding them where possible to artificially extend  $L$ , are the primary strategies for making the DFT and its inverse a good approximation to the Fourier transforms of equations (11) and (12).

#### 4. Comparison software

We will compare the outputs from GalSim against those from a completely independent piece of software, Chris Hirata’s spherical harmonic transform (SHT) code which is described in multiple papers (for example, Hirata et al. 2004). This does not use the flat-sky approach, but that should not make too much difference even for our  $L = 10$  deg. It is something to bear in mind if we start looking for agreement at a few % level on the largest  $\theta$  or smallest  $k$ . That software wants  $C_\ell(\ell)$  as its inputs.

#### 5. Tests of variances

We begin with tests of the shear variances from GalSim and the SHT code. The theoretical description for the variances was outlined in §2.

### 5.1. General considerations

As discussed in §2, most of our tests of the variance will focus on the sum of the components, rather than the variance of individual components. Also, for our grid to properly represent the theoretical power spectrum (and for the equations in §2 to be valid), we need to be well-sampled in  $k$  space, so we should not use functions that do unreasonable things like  $P(k) \propto k^{-2}$ .

Since we will want to check that the results behave properly when the grid changes, we will do all tests in this section with three different grids:

1. A standard GREAT10 grid, which has  $L = 10$  degrees and  $N = 100$ , so  $d = 0.1$  degree = 360 arcsec.
2. A grid with  $L = 5$  degrees and  $N = 50$ , thus preserving  $d$  and  $k_{\max}$ , while increasing  $k_{\min}$  (the Fourier-space grid spacing) by a factor of 2.
3. A grid with  $L = 10$  degrees and  $N = 50$ , thus doubling  $d$  and halving  $k_{\max}$ , while preserving the Fourier-space grid spacing ( $k_{\min}$ ) compared to the original case.

### 5.2. Variance for Gaussian $P(k)$

Our first test case is a Gaussian  $P(k)$ , i.e.,  $P(k) = P_0 e^{-\sigma^2 k^2/2}$ . Here both  $P_0$  and  $\sigma^2$  both have dimensions of angle<sup>2</sup>. By Eq. (10), this means that we expect

$$\text{Var}(\gamma) = \frac{4P_0}{(2\pi)^2} \left[ \left( \int_0^{k_{\max}} e^{-\sigma^2 k^2/2} dk \right)^2 - \left( \int_0^{k_{\min}} e^{-\sigma^2 k^2/2} dk \right)^2 \right] \quad (36)$$

$$= \frac{P_0}{2\pi\sigma^2} \left[ \left( \text{Erf}(k_{\max}\sigma/\sqrt{2}) \right)^2 - \left( \text{Erf}(k_{\min}\sigma/\sqrt{2}) \right)^2 \right]. \quad (37)$$

For each of the grids, we define the Gaussian  $\sigma$  such that there is essentially no power left at our  $k_{\max}$ :  $\sigma k_{\max} = 2.5$ , or  $\sigma = 286.5$  arcsec for the first two grids and  $\sigma = 573$  arcsec for the last grid. Given how large  $\sigma k_{\max}$  is, in all cases,  $\text{Erf}(k_{\max}\sigma/\sqrt{2}) = 0.988$ . The resulting values of  $\sigma k_{\min}$  for the three grids are 0.05, 0.1, and 0.05, or  $\text{Erf}(k_{\min}\sigma/\sqrt{2}) = 0.04, 0.08, \text{ and } 0.04$  (since these are squared in the above expression, they don't end up mattering much). With  $P_0 = 1$  arcsec<sup>2</sup>, the predicted variances for the three grids are  $1.89 \times 10^{-6}$ ,  $1.88 \times 10^{-6}$ , and  $4.72 \times 10^{-7}$ .

The code to do this once is:

```
import galsim
import numpy as np
test_ps = galsim.PowerSpectrum(lambda k : np.exp(-0.5*((286.5*k)**2)))
g1, g2 = test_ps.buildGrid(grid_spacing=360., ngrid=100)
```

```
print np.var(g1), np.var(g2), np.var(g1)+np.var(g2)
g1, g2 = test_ps.buildGrid(grid_spacing=360., ngrid=50)
print np.var(g1), np.var(g2), np.var(g1)+np.var(g2)
test_ps = galsim.PowerSpectrum(lambda k : np.exp(-0.5*((573.0*k)**2)))
g1, g2 = test_ps.buildGrid(grid_spacing=720., ngrid=50)
print np.var(g1), np.var(g2), np.var(g1)+np.var(g2)
```

We actually do this 1000 times to beat down the noise in the resulting variances.

The results are  $1.89 \times 10^{-6}$ ,  $1.89 \times 10^{-6}$ , and  $4.72 \times 10^{-7}$  in the last case. The results are therefore within 0.5% of the theoretical predictions.

The variance is fairly evenly divided between components, but the variance in  $\gamma_2$  tends to be larger than the variance of  $\gamma_1$  by 3–4%. This is likely because the  $P(k)$  emphasizes large scales, where the grid genuinely looks different along the diagonals as it does along the coordinate axes. It’s a feature of using grids to represent shears drawn randomly from a power spectrum with finite  $P_E$  but with  $P_B = 0$ , not a bug. If we set  $P_B = P_E$  (unlike in the above example where  $P_B = 0$ ) then this difference between the variances of  $\gamma_1$  and  $\gamma_2$  vanishes.

### 5.3. Variance for flat $P(k)$

A flat  $P(k)$  has a worrisome amount of power at large  $k$ , so we use a modified version of it: We use  $P(k) = P_0$  for  $k \leq k_{\text{lim}}$ , where  $k_{\text{lim}} < k_{\text{max}}$  for all the grids; and we set  $P(k > k_{\text{lim}}) = 0$ . Using Eq. (10), we expect

$$\text{Var}(\gamma) = \frac{4P_0}{(2\pi)^2} \left[ \frac{1}{4} \int_0^{k_{\text{lim}}} 2\pi k \, dk - k_{\text{min}}^2 \right] \quad (38)$$

$$= \frac{P_0}{\pi^2} \left( \frac{\pi}{4} k_{\text{lim}}^2 - k_{\text{min}}^2 \right). \quad (39)$$

For the set of grids from the previous test,  $k_{\text{min}}$  is 0.000175, 0.00035, and 0.000175 arcsec $^{-1}$ . We will set  $k_{\text{lim}} = 10k_{\text{min}}$ , so we can write

$$\text{Var}(\gamma) = \frac{(25\pi - 1)P_0 k_{\text{min}}^2}{\pi^2}. \quad (40)$$

With  $P_0 = 1$ , we expect shear variances that are  $2.41 \times 10^{-7}$ ,  $9.62 \times 10^{-7}$ , and  $2.41 \times 10^{-7}$ .

The code is

```
import galsim
import numpy as np
def pfunc1(k):
```

```

    parr = np.zeros_like(k)
    parr[k<=0.00175] = 1.
    return parr
def pfunc2(k):
    parr = np.zeros_like(k)
    parr[k<=0.0035] = 1.
    return parr
test_ps1 = galsim.PowerSpectrum(pfunc1)
test_ps2 = galsim.PowerSpectrum(pfunc2)
g1, g2 = test_ps1.buildGrid(grid_spacing=360., ngrid=100)
print np.var(g1), np.var(g2), np.var(g1)+np.var(g2)
g1, g2 = test_ps2.buildGrid(grid_spacing=360., ngrid=50)
print np.var(g1), np.var(g2), np.var(g1)+np.var(g2)
g1, g2 = test_ps1.buildGrid(grid_spacing=720., ngrid=50)
print np.var(g1), np.var(g2), np.var(g1)+np.var(g2)

```

Since the variances are noisy, we averaged the results over 10000 realizations<sup>2</sup>, and found  $2.44 \times 10^{-7}$ ,  $9.75 \times 10^{-7}$ , and  $2.44 \times 10^{-7}$ . These are all  $\sim 1.3\%$  above the theoretical prediction. Since the overall behavior is correct when we change the grid size and spacing, it seems possible that this small discrepancy comes from some finite-gridding effect.

## 6. Test of full $P(k)$

We use a WMAP7 LCDM prediction for the cosmic shear signal for a sample with  $z_{\text{med}} \sim 0.55$  as an input to both the SHT code and ours. For this test we use a grid with  $L = 10$  degrees (as before), but  $N = 50$  (i.e.,  $d$  gets doubled), which means a one-dimensional  $k_{\text{max}} = \ell = 900$  radians<sup>-1</sup>.

Using the SHT code (§4), we made gridded shears for  $P_E = P(k)$  and  $P_B = 0$ ;  $P_B = P(k)$  and  $P_E = 0$ ; and  $P_E = P_B = P(k)$  (5 realizations of each). For GalSim, since it is much faster, we averaged over several hundred realizations. It is crucial to inform GalSim that the inputs have units of radians. For the SHT code, we instruct it to zero out the power spectrum for  $\ell > 900$  to avoid spurious power in  $E$  and  $B$  modes due to aliasing.

The python script `test_pk.py` in `devel/external/test_gridshear/` does the following:

1. Generates shears according to this PS using GalSim.

---

<sup>2</sup>This takes about 1 minute to run on a single CPU.

2. Runs the GREAT10 power spectrum code on both, and averages it over many noise realizations.

The python script `test_pk_sht.py` in that directory does the following:

1. Manipulate outputs of the SHT code to be consistent with expectations (including one sign flip for  $e_1$ ).
2. Runs the GREAT10 power spectrum code on it.

Finally, `plot_pk_test.py` in that directory plots the original and simulated  $P(k)$  based on these files. The results for the three cases (input  $P_E$ , input  $P_B$ , and input  $P_E = P_B$ ) are in Figures 1, 2, and 3.

We can conclude several things from these figures:

- The SHT code gives roughly a consistent shear power spectrum compared to our GalSim outputs.
- We don't see  $E$  vs.  $B$  leakage at any significant level. The amplitudes and scaling of our output power spectra with  $\ell$  are approximately correct.
- While the big-picture results seem good, there are some finer details that require investigation, for example the apparent deficit in power at low  $\ell$ .

To address the last point, the simplest possible test is to change the  $\ell$  binning in the PS estimation code. This will let us check whether we are encountering some finite-binning effects in the PS estimation. The original calculations had 20  $\ell$  bins; the new one uses 50 within the same  $\ell$  range. To beat down the noise, we used 400 realizations of the shears from GalSim, instead of 20 as before. The result is shown in Fig. 4. It is clear that the results are, as compared to Fig. 1, closer to the theory. In particular, the amplitude *and* slope are both close to theory for  $\ell > 100$ . Note that the jitter in that curve does not go away if we use more realizations. This could have to do with the exact locations of the annular  $\ell$  bins in the PS estimation code, as compared to the finite set of  $\ell$  modes that are probed by our grid.

Since the log plot makes it hard to see how large differences between theory and the GalSim results are, Fig. 5 shows the ratio between the GalSim outputs and the theory. For  $\ell < 100$ , the GalSim results are too low by  $\sim 15\%$ . For  $\ell > 100$ , the GalSim outputs seems to give power spectra that are several percent too low. This finding suggests that users *must* account for the effects of finite  $\ell$ -binning on the theoretical power spectrum when generating the shears, unless they can choose sufficiently fine  $\ell$  bins to minimize this problem. In support of this claim that finite gridding is responsible, we found that with a grid that is doubled in size (and hence a Fourier-space grid that

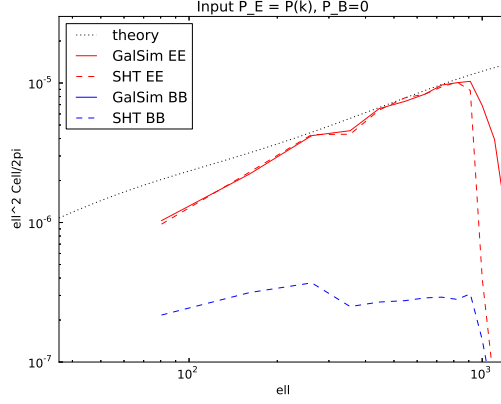


Fig. 1.— Output shear power spectra (plotted as the dimensionless  $\Delta^2$ ) for the grids described in Sec. 6, where the input  $P_E$  is a realistic cosmological one (shown as the ‘theory’ line on the plot) and the input  $P_B = 0$ . The results for GalSim and the comparison SHT code are both plotted.

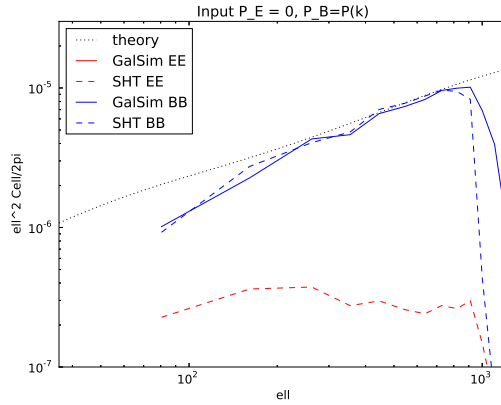


Fig. 2.— Output shear power spectra (plotted as the dimensionless  $\Delta^2$ ) for the grids described in Sec. 6, where the input  $P_B$  is a theoretical one and the input  $P_E = 0$ . The results for GalSim and the comparison SHT code are both plotted.

is twice as finely spaced), the ratio of observed to expected power spectrum is closer to 1 (but still 3% too low).

In detail, finite-gridding effects can arise because our gridded approach amounts to estimating the power at specific  $k_1$  and  $k_2$  values (or rather in  $k_1$  and  $k_2$  bins of width  $\Delta k$ ). When the PS estimator gets the power using the DFT approach, it’s essentially calculating these as  $P(k = \sqrt{k_1^2 + k_2^2})$  which are, again, defined at a set of specific values. However, we then tell the PS estimator “tell me the power in some set of bins in  $\log k$ ”, the edges of which are not aligned in any particular way with respect to our actual  $k$  values at which we have estimated the power using the DFT approach. The PS estimator gets the power in each of our logarithmic bins via summation over the  $P(k)$  for all  $k$  values that happen to fall into that logarithmic bin. This means there is some interplay between the grid geometry (determining the  $k$  values for which we’ll have  $P(k)$ ) and the choice of log bins, which could result in jitter depending on how the two relate. A future version of this document will show what happens if we explicitly account for this when comparing with the theory.

We have confirmed that the results are fairly robust to the grid spacing, for example by making the grid a factor of two more finely spaced (and extending the WMAP7  $P(k)$  as a constant above  $\ell = 2000$  so that we can do this) and confirming that the results agree with Fig. 1.

A final comment about noise: shape noise and the effect of pixel noise in galaxy shape measurements add a term to the power, however here we are doing tests of just the cosmological shear without either of the above effect, so that is why it is not included in the above formalism. A realistic test of power spectra from simulated images would have to include these effects.

The deficit in power at low  $\ell$  is likely the same phenomenon seen in the CMB: the assumption of Gaussian distributions for  $C_\ell$  stops being true because there aren’t enough samples for the central limit theorem to apply. As a result, using the RMS  $a_{\ell m}$  as the inputs to the shear generation code (which is what we are effectively doing) starts to be wrong. The simplest solution to this problem is to use simulations to predict the magnitude of the effect, and then compare results with that prediction. The same statement applies to other limitations such as finite-gridding effects. In particular, it would not be reasonable to compare the recovered PS with the theoretical one as a precise test of shear estimation, since all the aforementioned effects are much larger than the level at which we wish to test shear estimation. Instead, the fair comparison would be to compare the observed curves above (that come from running the idealized shear values on the grid through our PS estimator) with the ones that challenge participants reconstruct from the galaxy images.

As an example of how this could work in practice, Figs. 6 and 7 show the results of using the power spectrum estimation software that is in GalSim on the outputs of the GalSim lensing engine. In Fig. 6, we show the results of simulating shears with  $P_B = 0$  and  $P_E$  that comes from a cosmological shear power spectrum. The GalSim power spectrum estimation software is able to account for the effects of the finite size of the logarithmic  $\ell$  bins used for power spectrum estimation and their relation to our discrete grid of  $\ell$  values, producing a “theory” curve that includes those

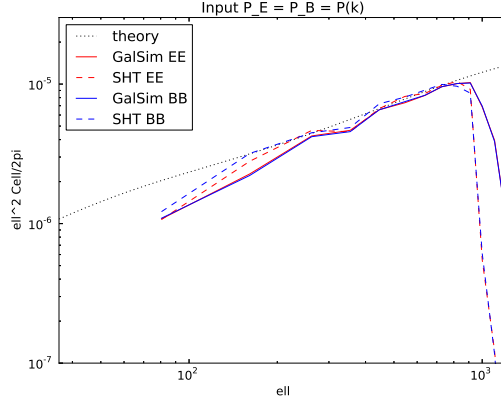


Fig. 3.— Output shear power spectra (plotted as the dimensionless  $\Delta^2$ ) for the grids described in Sec. 6, where the input  $P_E = P_B$  is shown as the ‘theory’ line. The results for GalSim and the comparison SHT code are both plotted.

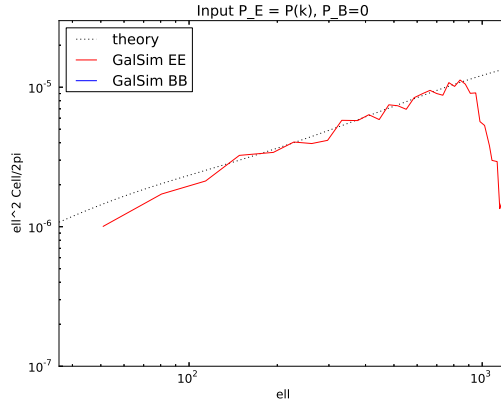


Fig. 4.— Output shear power spectra (plotted as the dimensionless  $\Delta^2$ ) for the grids described in Sec. 6, where the input  $P_E$  is a realistic cosmological one (shown as the ‘theory’ line on the plot) and the input  $P_B = 0$ . The results for GalSim and the comparison SHT code are both plotted, but for GalSim we used 50  $\ell$  bins in the PS estimation, rather than 20 as in Fig. 1.



effects directly. It is clear that the estimated power spectrum is closer to that binned theory estimate than it is to the ideal theory curve, which makes sense. Fig. 7 shows the ratio of the estimated power to the ideal and binned theory curves. Use of the binned theory curve has reduced the residuals to a maximum of 3% (more typically 1%), but since the shear systematics we are trying to detect are comparable in size to those residuals, we should compare with the red curve in Fig. 6 rather than the idealized or binned theory when evaluating shear estimation methods.

## 7. Shear power on larger scales than our grid

It is not clear that we should really be enforcing  $P(k = 0) = 0$ , i.e., no power below our  $k_{\min}$ . This is a valid condition for the full-sky power spectrum, but will not in general be valid for a small patch of the sky, due to cosmic variance. In order to include this sampling variance, it would be preferable to first define a much larger real-space grid than we actually need, so that the Fourier-space grid has much smaller  $k_{\min}$  and therefore has information about larger-wavelength modes than are included by our limited real-space grid. However, this limitation is only a problem if we are checking quantities like the shear correlation function or its value at  $\theta = 0$ , i.e., the shear variance. If we are testing the ability to recover a power spectrum  $P(k)$  defined at the values of  $k$  that are accessible to our grid, the  $P(0) = 0$  condition that we have imposed should be irrelevant. Nonetheless, we may wish to modify the lensing engine to check whether the power function is defined for  $0 < k \leq k_{\min}$ , and assign some appropriately-weighted integral over that range as  $P(k = 0)$ .

Figure 8 illustrates the impact of the limitation in the range of  $k$  modes represented by our grid. In the left panel, a comparison of the theoretical shear correlation functions  $\xi_+$  and  $\xi_-$  (in the case of infinite  $k$  range when integrating over the Bessel functions in Eq. 3) versus the observed one after generating shears on our default grid reveals that the limitation in  $k$  modes represented by our grid leads to substantial reduction in large-scale shear correlations compared to the theory. In the right panel, the same quantities are shown, but this time the grid has been expanded by a factor of 10, thus lowering the minimum  $k$  value for the grid by a factor of 10. In this case, the theoretical and observed correlation functions are nearly identical, illustrating that the limitation in  $k_{\min}$  for the gridded representation in Fourier space was the key issue in getting the correlation function correct on large scales in the left panel. The current version of GalSim thus has a warning about this band-limitation on the power spectrum in the docstrings for the lensing engine. Future work should allow the user to circumvent this limitation and properly represent the shear correlation function, at the expense of increased computation time.

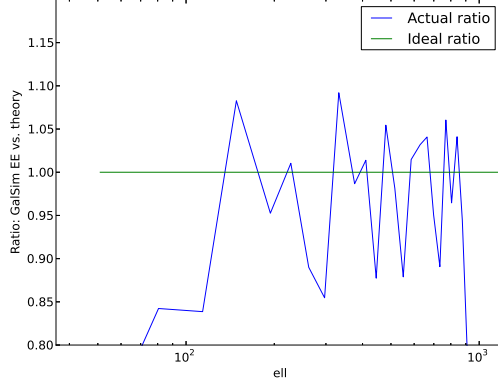


Fig. 5.— Ratio of GalSim EE PS vs. theory from Fig. 4.

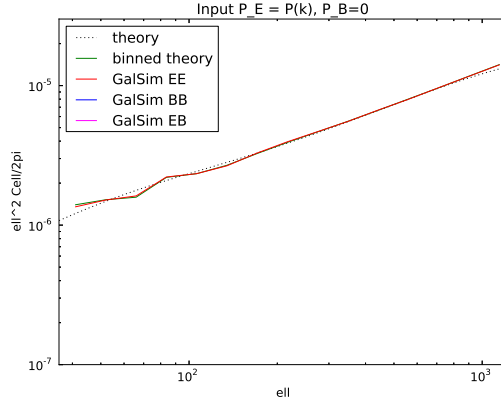


Fig. 6.— Output shear power spectra (plotted as the dimensionless  $\Delta^2$ ) for the grids described in Sec. 6, where the input  $P_E$  is a realistic cosmological one (shown as the ‘theory’ line on the plot) and the input  $P_B = 0$ . Results are shown using the GalSim power spectrum estimation software, and include a “rebinned theory” curve that accounts for the effect of our finite-sized  $\ell$  bins on the theory prediction

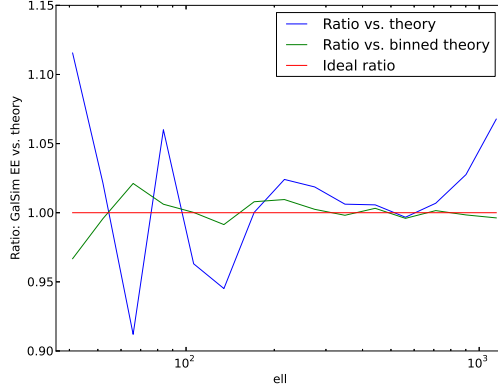


Fig. 7.— Ratio of GalSim EE PS vs. theory from Fig. 6.

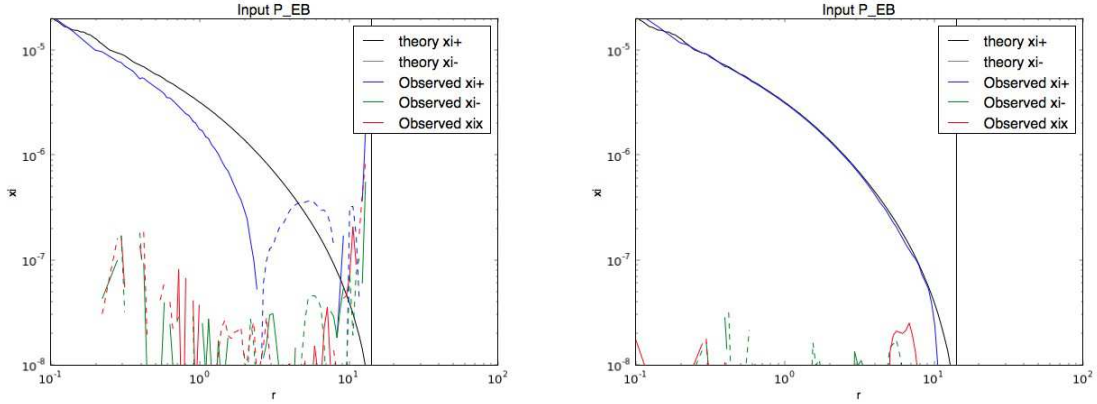


Fig. 8.— *Left:* Shear correlation functions  $\xi_+$  and  $\xi_-$  that should correspond to some reasonable input  $P(k)$ , and the observed shear correlation functions after generation of shears on our default grid. *Right:* Same as left, but after artificially extending the grid by a factor of 10 in length, so that the minimum value of  $k$  that can be represented is reduced by a factor of 10.